

1 **A free, open-source method for automated mapping of quantitative mineralogy from energy-dispersive X-**
2 **ray spectroscopy scans of rock thin sections**

3 Miles M. Reed¹, Ken L. Ferrier¹, William O. Nachlas¹, Bil Schneider¹, Chloé Arson², Tingting Xu³, Xianda Shen^{4,5},
4 and Nicole West⁶

5 ¹Geoscience, University of Wisconsin-Madison, United States

6 ²Civil and Environmental Engineering, Cornell University, United States

7 ³Hopkins Extreme Materials Institute, John Hopkins University, United States

8 ⁴Key Laboratory of Geotechnical and Underground Engineering of Ministry of Education, Tongji University, China

9 ⁵Department of Geotechnical Engineering, Tongji University, China

10 ⁶Independent Researcher

11 *Correspondence to:* Miles Reed (miles.reed@wisc.edu)

12 **Abstract**

13 Quantitative mapping of minerals in rock thin sections delivers data on mineral abundance, size, and spatial
14 arrangement that are useful for many geoscience and engineering disciplines. Although automated methods for
15 mapping mineralogy exist, these are often expensive, associated with proprietary software, or require
16 programming skills, which limits their usage. Here we present a free, open-source method for automated
17 mineralogy mapping from energy dispersive spectroscopy (EDS) scans of rock thin sections. This method uses a
18 random forest machine learning image classification algorithm within the QGIS geographic information system
19 and Orfeo Toolbox, which are both free and open source. To demonstrate the utility of this method, we apply it to
20 14 rock thin sections from the well-studied Rio Blanco tonalite lithology of Puerto Rico. Measurements of
21 mineral abundance inferred from our method compare favourably to previous measurements of mineral
22 abundance inferred from X-ray diffraction and point counts on thin sections. The model-generated mineral maps
23 agree with independent, manually-delineated mineral maps at a mean rate of 95%, with accuracies as high as
24 96% for the most abundant mineral (plagioclase) and as low as 72% for the least abundant mineral (apatite) in
25 these samples. We show that the default random forest hyperparameters (i.e., tuneable settings that control
26 behaviour) in Orfeo Toolbox yielded high accuracy in the model-generated mineral maps, and we demonstrate
27 how users can determine the sensitivity of the mineral maps to hyperparameter values and input features. These
28 results show that this method can be used to generate accurate maps of major minerals in rock thin sections using
29 entirely free and open-source applications.

31 **1 Introduction**

32 Minerals are the fundamental units of rocks and many engineered materials (Perkins, 2020; Callister and
33 Rethwisch, 2020). Improving the quantification of mineral properties is a longstanding research objective in
34 industry and academic research (Pirrie and Rollinson, 2011), given the importance of mineral properties in
35 chemical weathering (e.g., Hilton and West, 2020), rock damage (e.g., Shen et al., 2019; Xu et al., 2022),
36 planetary evolution (e.g., Hazen et al., 2008), crustal deformation (e.g., Burgmann and Dresen, 2008), and
37 nutrient supply (e.g., Callahan et al., 2022). Quantitative automated mineralogy, the computerized mapping of
38 minerals across a sample, results in measurements of mineral modal abundance, mineral grain size and shape, and
39 the spatial arrangement of minerals amongst one another (Sutherland et al., 1988; Sutherland & Gottlieb, 1991;
40 Gu, 2003; Schulz et al., 2020). Modal abundance is useful because it can yield information on the sedimentary
41 and tectonic environments in which the rock formed (Harlov et al., 1998; Hupp and Donovan, 2018), while the
42 spatial arrangement of minerals in a rock, termed rock fabric, can yield further data on mechanical anisotropy and
43 paleo-environmental conditions during the rock's formation and metamorphism (Přikryl, 2006; Bjørlykke, 2014).
44 Simultaneous quantification of modal mineralogy and detailed mapping of the spatial arrangement of minerals in
45 an automated manner, or automated mineralogy, is thus a key tool for investigating many geologic processes.
46 Wide adoption of automated mineralogy techniques are limited by the prohibitive cost or programming skills
47 required to use many automated mineralogy software applications, so this technique has been mostly restricted to
48 ore characterization, resource processing, and petroleum geology (Nikonow and Rammlmair, 2017; Schulz et al.,
49 2020).

50

51 In practice, automated mineralogy methods use a combination of image analysis and classification methods to
52 identify minerals from elemental composition data (or their derivatives), which can be collected with a variety of
53 analytical methods, including energy dispersive X-ray spectroscopy (EDS), micro-X-ray fluorescence (μ -XRF),
54 and laser-induced breakdown spectroscopy (LIBS) (Nikonow et al., 2019). Automated mineralogy is being
55 slowly adopted by researchers outside of resource extraction for combined modal analysis of bulk mineralogy,
56 estimates of grain size distribution, and mineral association (Han et al., 2022), which can be useful in a variety of
57 disciplines such as petrology, applied geochemistry, and rock mechanics (Sajid et al., 2016; Elghali et al., 2018;
58 Rafiei et al., 2020).

59

60 Automated mineralogy from EDS with the aid of back-scattered electron (BSE) imaging has been developing
61 since the 1980s and has grown alongside advances in scanning electron microscopy (SEM) and image processing
62 algorithms (Miller et al., 1983; Fandrich et al., 2007). Commercial automated mineralogy systems are available

63 as integrated hardware-software systems or as standalone software packages which are combined with scanning
64 electron microscopes (Schulz et al., 2020). Some systems only work with certain scanning electron microscopes
65 and detectors from the same company QEMSCAN (Gottlieb et al., 2000), FEI-MLA (Fandrich et al., 2007), and
66 TESCAN TIMA-X (Hrstka et al., 2018). Others are purely software-based solutions which are integrated with
67 various SEMs: ZEISS Mineralogic, Oxford AZTecMineral, and Thermo-Scientific MAPS Mineralogy. The price
68 of hardware and software upgrades required to accommodate these systems renders them cost prohibitive to
69 many labs outside the resource extraction industry (Nikonow and Rammlmair, 2017). All systems have some
70 general ability to classify EDS spectra based on a database of pre-defined and/or customizable mineral spectra
71 standards (Schulz et al., 2020). Since the underlying software is proprietary, no source code is available for these
72 systems, and details on how they use spectra to classify minerals are sparse to non-existent (Kuelen et al., 2020).
73 Furthermore, the accuracy of mineral prediction from these systems has rarely been quantified (Blannin et al.,
74 2021).

75
76 To date, several open-source (i.e., source code is available and modifiable) automated mineralogy solutions have
77 been implemented. Ortolano et al. (2014, 2018) predicted modal mineralogy and mapped minerals from a
78 multistep workflow involving principal component analysis, maximum likelihood classification, and multi-linear
79 regression performed on EDS or WDS spectral data using the Python extension within ArcGIS. Li et al. (2021)
80 used a variety of legacy machine-learning and deep-learning models to classify minerals in oil reservoir rocks
81 using mineral maps generated from proprietary software as training data. In terms of image classification, deep-
82 learning methods are state of the art but currently require the user to be relatively adept at programming and
83 knowledgeable of the computer vision principles employed (Khan et al., 2018; Zhang et al., 2019). A method that
84 requires little to no programming ability would allow more users to benefit from automated mineralogy data. An
85 example of this approach is XMapTools by Lanari et al. (2014), a graphical, open-source automated mineralogy
86 solution with multiple machine-learning classification algorithms within a standalone, MATLAB-based
87 environment.

88
89 Random forest (RF) classification is a supervised classification algorithm (i.e., the user generates training data) in
90 which an ensemble of decision trees produces a majority vote that assigns a thematic classification to unknown
91 data (Breiman, 2001). Each decision tree within the ensemble is trained on a random sample of the training data
92 using only a set number of random features at each branch (Cutler et al., 2011). During prediction, for each
93 decision tree, unknown data traverses a sequence of rule-based branches which culminate in the assignment of a

94 predicted class (Breiman, 2001). Each tree gets one vote for each pixel; the predicted class with the most votes is
95 assigned to the unknown data. There are several reasons why RF classification is useful for automated
96 mineralogy mapping. It is well suited for accommodating unbalanced training data and nonparametric data
97 distributions (Maxwell et al., 2018), which are common in rock samples due to large differences in relative
98 mineral abundances and elemental intensities (Ahrens, 1954). In addition, recent work showed that RF
99 classification performed better than other legacy machine-learning algorithms (e.g., support-vector machines;
100 Hearst et al., 1998) in mineral classification of reservoir rocks (Li et al., 2021).

101

102 The main goal of this study is to present a new, user-friendly quantitative automated mineralogy method that we
103 developed and implemented within QGIS, a free and open-source geographic information system. Unlike
104 previous methods, the method presented here uses only freely available and open-source applications, and it
105 requires no programming by the user. We use the free and open-source Orfeo Toolbox plugin for QGIS
106 (Grizonnet et al., 2017) to predict thin-section scale bulk mineralogy from EDS elemental intensity data using a
107 RF image classifier (Breiman, 2001). Situating the workflow within a GIS environment has advantages over
108 standalone programs such as direct access to raster and vector manipulation and analysis tools and database
109 management (Tarquini and Favalli, 2010; Berrezueta et al., 2019). Furthermore, we present an overview of the
110 automated mineralogy method and apply it to a set of rock samples from the Rio Blanco tonalite to demonstrate
111 the method's utility. By outlining an easy-to-use and open-source solution, we intend to provide an automated
112 mineralogy method to a broader community of users.

113

114 **2 Overview of the method**

115

116 The goal of our automated mineralogy method is to produce quantitative mineralogy maps of rock thin sections
117 solely from EDS data acquired using a SEM. Here in Section 2, we briefly summarize each step needed to reach a
118 predicted mineral map. In Section 3, we demonstrate how to use the method by applying it to a set of rock thin
119 sections, during which we elaborate on the choices users need to make and the functions they need to use during
120 each step. We also provide a detailed step-by-step guide in the supplementary information (Reed et al., 2024).

121

122 The starting point for this method is elemental rasters derived from EDS-generated scans of rock thin sections.
123 For the purposes of our method, we take these scans as already measured and in hand. Generating such scans
124 requires preparing thin sections and analyzing them with a scanning electron microscope, both of which are done

125 by established procedures (Goldstein et al., 2018). The necessary output from such scans are rasters of elemental
126 intensity (counts/eV), one for each element of interest (e.g., Ca, Na, K, etc.). After the EDS elemental intensity
127 rasters have been generated, all the remaining steps in the method are conducted in QGIS. No programming is
128 required in any step. Instead, users need only be familiar with QGIS and their samples.

129

130 The first step involves importing the raw elemental intensity rasters into QGIS with no coordinate reference
131 system (Fig. 1a). This also involves compiling a list of all the minerals that will be mapped in the thin section,
132 which can be assessed based on prior knowledge, literature, and examination of EDS spectra. Our method is not
133 viable for those thin sections from completely unknown lithologies that resist efforts to identify minerals under
134 the microscope and/or manual examination of EDS data. As we describe in Section 4, we recommend restricting
135 this to minerals with sufficiently high abundance ($>0.1\%$) to be adequately trained upon. For those workers that
136 require high accuracy in very low abundance minerals, our method is not advisable.

137

138 The second step is to smooth the raw elemental intensity rasters (Fig. 1b). This is useful because EDS-generated
139 elemental intensity rasters are subject to noise, which can arise through electron beam interactions with the
140 sample (Goldstein et al., 2018). As we describe in Section 4.3, we found that this smoothing step was best done
141 with a 7-pixel radius circular mean filter, in which each pixel is assigned the mean value of the surrounding
142 pixels in a circular window (Gonzalez and Woods, 2018). We performed this on intensity rasters from the
143 example samples we applied our method to in Section 3. For this, we used the free and open-source System for
144 Automated Geoscientific Analyses (SAGA) plugin for QGIS (Conrad et al., 2015).

145

146 The third step is to gather the smoothed elemental intensity rasters into a virtual raster, a type of container for
147 multiple rasters, with one band for each element of interest (Fig. 1c). For example, if the user chooses to import
148 elemental intensity rasters for six elements, as we did in the application of this method to our samples in Section
149 3, this will result in a virtual raster with six bands. For this, we used the Geospatial Data Abstraction Library
150 (GDAL/OGR contributors, 2022), which is a standard library in QGIS.

151

152 The fourth step is to train a RF image classification model on the virtual raster (Fig. 1d). This requires generating
153 a large number (~hundreds) of small polygons on the virtual raster. Each of these small polygons must lie within
154 a single mineral, which the user must identify and assign to the polygon. Collectively, these small polygons must
155 cover all the minerals of interest in the thin section in sufficient number to train the RF model. If the user wishes

156 to assess the accuracy of the RF-predicted mineral map to a manually mapped portion of the thin section, we
157 recommend restricting the location of these small training polygons to a relatively small portion of the thin
158 section (~10-20% by area). This will ensure that other portions of the thin section can be mapped manually to
159 compare against the RF-predicted mineral map. If the user does not wish to conduct such an accuracy assessment
160 after the RF-predicted mineral map is complete, then these small training polygons can be generated anywhere
161 across the entire thin section.

162

163 After the RF model has been trained, the fifth step is to apply the trained RF model to the entire virtual raster
164 (Fig. 1e). During this step, the RF model assigns a mineral class to every pixel in the virtual raster, which yields a
165 mineral map for the entire thin section. For these RF modeling steps, we used the free, open-source Orfeo
166 Toolbox plugin for QGIS (Grizonnet et al., 2017).

167

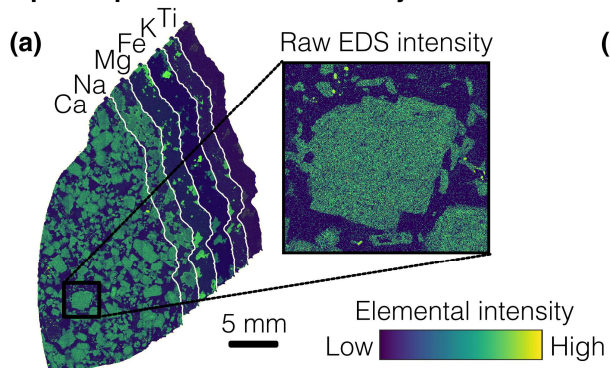
168 The sixth and final step is to denoise the RF-generated mineral map (Fig. 1f). For this, we applied a circular
169 majority filter using the SAGA plugin for QGIS, in which each pixel is assigned the modal value of the
170 surrounding pixels in a circular window (Gonzalez and Woods, 2018). As we describe in Section 4.3, we found
171 that this was best done with a 10-pixel radius majority filter in the example samples we applied this to in Section
172 3. This eliminates most isolated pixels within larger groups of pixels of a uniform predicted mineral and rare
173 pixels that were not classified due to voting ties (Ortolano et al., 2018; Nikonow et al., 2019)

174

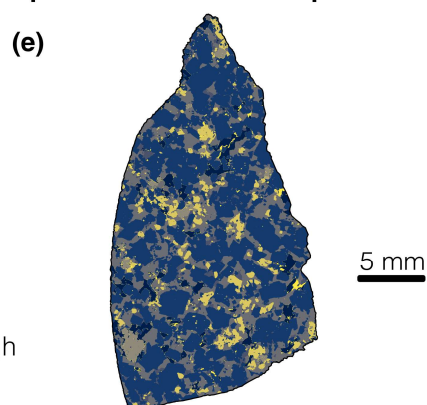
175 At this stage, the RF-predicted mineral map is complete. It can now be examined or manipulated according to the
176 user's needs. For instance, the mineral map can be converted from a raster to a vector form to facilitate
177 measurement of mineral grain size and other properties (Section 5.2).

178

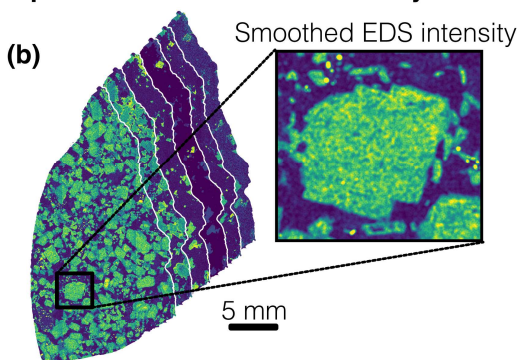
Step 1: Import elemental intensity rasters



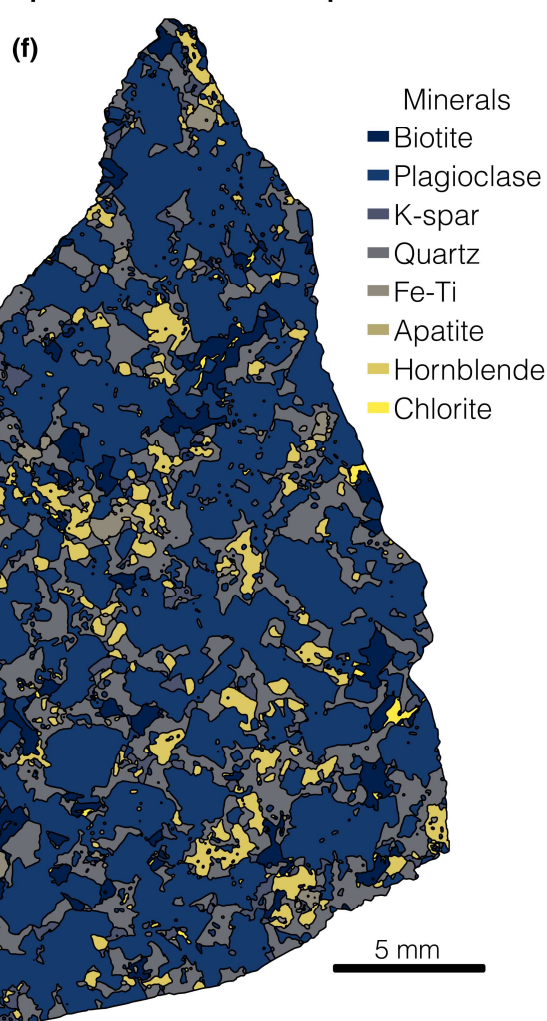
Step 5: Create mineral map



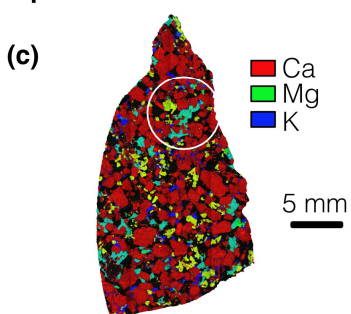
Step 2: Smooth elemental intensity rasters



Step 6: Smooth mineral map



Step 3: Create virtual raster



Step 4: Train random forest model

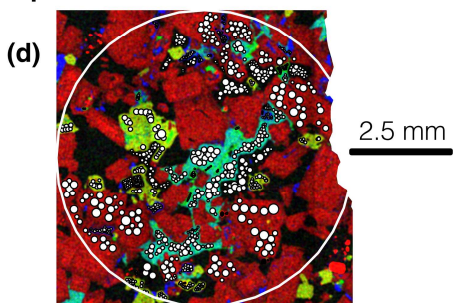


Figure 1. Example application of the automated mineralogy method. (a) Step 1: Import raw elemental intensity rasters (Ca, Na, Mg, Fe, K and Ti) into QGIS. Here, the rasters shown are for the thin-section sample 1-13a. The zoomed-in view of the Ca raster exemplifies the short-wavelength noise in the elemental rasters. (b) Step 2: Smooth each elemental intensity raster with a circular mean filter. The zoomed-in view shows that this filter has eliminated much of the short-wavelength noise that was in the raw elemental rasters. (c) Step 3: Create a virtual raster by combining the smoothed elemental rasters into a single image container with bands for each element. The white circle shows the area within which polygons were generated to train the random forest (RF) model in Step 4. (d) Step 4: Within the training area boundary in the virtual raster (large white circle, as in Step 3), draw a series of small polygons (here, small white circles). Each polygon must lie within a single known mineral, and collectively these small polygons must sample all mineral of interest (here, plagioclase feldspar, quartz, hornblende, biotite, potassium feldspar, Fe-Ti oxides, apatite, and chlorite). These polygons collect the pixel-level data on which the RF model will be trained. (e) Step 5: Apply the trained RF model to the entire sample to create a thin section-scale mineral map. (f) Step 6: Smooth the RF-predicted mineral map with a circular majority filter.

179

180

181 **3 Application of the method**

182

183 **3.1 Preparation of rock thin sections from the Luquillo Critical Zone Observatory**

184 To demonstrate the utility of the method described in Section 2, we applied it to 14 thin sections of Rio Blanco
 185 tonalite from the Luquillo Critical Zone Observatory (LCZO) in Puerto Rico, United States, a site that has been
 186 the subject of substantial research on the weathering of igneous rocks into saprolite and soil (White et al., 1998;
 187 Riebe et al., 2003; Stallard and Murphy, 2012; Brocard et al., 2023). The lithology is a phaneritic, plutonic
 188 igneous rock with some evidence of low-grade hydrothermal alteration (Speer, 1984). The Rio Blanco tonalite
 189 provides an ideal case study because mineral abundance has been characterized previously via quantitative X-ray
 190 diffraction (XRD) and point counting modal analysis (i.e., systematic manual identification and counting under
 191 microscope; Ingersoll et al., 1984), which indicated the rock consists of plagioclase feldspar (andesine), quartz,
 192 biotite, hornblende, potassium feldspar, magnetite, apatite, and chlorite (Murphy et al., 1998; Buss et al., 2008;
 193 Ferrier et al., 2010).

194

195 To ready the samples for EDS, 14 petrographic thin sections were prepared on 27 x 46 mm glass slides from
196 bedrock core quarters collected from the Rio Icacos catchment within the LCZO (Comas et al., 2019). The
197 samples ranged in area from 34.7 to 139.5 mm². Four samples are composed of weathered rock nearer to the
198 surface while the rest are more pristine bedrock (Orlando et al., 2016). From each core depth, two thin sections
199 were prepared in vertical and horizontal orientations. Our own preliminary optical microscopy observations
200 revealed that these samples contained abundant plagioclase, quartz, hornblende, and biotite, which is consistent
201 with previous modal analyses (Murphy et al., 1998; Buss et al., 2008).

202

203 **3.2 Measuring elemental intensity in thin sections with energy dispersive spectroscopy**

204 Each thin section was mapped with energy dispersive X-ray spectroscopy (EDS) using a Hitachi S-3400 VP-
205 SEM with a thermionic tungsten electron source equipped with an Oxford Instruments X-Act 10 mm² silicon drift
206 detector receiving X-rays across 2048 spectral bands. The EDS detector acquires a spectrum showing the energy
207 and intensity of characteristic X-rays emitted from the sample to determine the atomic composition of the sample
208 within the analysis volume of the primary beam (Goldstein et al., 2018). For the measurements on our thin
209 sections, the instrument and accompanying software produced full thin-section elemental intensity maps
210 (counts/eV) at a resolution of 4 µm/pixel, which was determined by the beam step size. EDS data were acquired
211 with accelerating voltage of 15 kV and beam current of ~10 nA. EDS process time (also known as ‘time constant’
212 by some manufacturers) was 4, which is an intermediate value that balances acquisition time and data quality.
213 EDS acquisition time was ~3.5 hours for each thin section.

214

215 From the EDS analysis application included with this instrument (AZtec), we exported six TIF files for each
216 sample (Fig. 1a) consisting of full-resolution elemental intensity rasters for the elements of interest (Ca, Na, K,
217 Mg, Fe and Ti). These rasters contain the X-ray counts of elemental intensity at each pixel and have a mean size
218 of over 20 megapixels over the 14 studied thin sections. We selected these elements because they are present in
219 varying abundance in the minerals within the Rio Blanco tonalite and, hence, are useful for distinguishing among
220 the minerals in these samples. For example, K, Mg, Fe, and Ti are present at high abundance in biotite (Dong et
221 al., 1999) but are present at low abundance in other major minerals in this lithology (e.g., plagioclase feldspar,
222 quartz). Our initial attempts at classification showed that the inclusion of rasters of Si and Al had no effect on
223 classification accuracy, so we did not include them here.

224

225 This method requires a list of minerals present in the samples for both training of and prediction by the RF
226 models (Steps 4 and 5 in Section 2). Such a list can be obtained in a variety of ways, including prior studies of
227 qualitative mineralogy of the host lithology or mineral identification from optical microscopy on the sample thin
228 sections. For the 14 samples analyzed here, we generated a list of minerals by inspecting the EDS-generated X-
229 ray spectral data within Oxford AZtec, a proprietary software package integrated with the SEM that we used to
230 measure EDS scans of our samples. From these spectra we identified plagioclase feldspar, quartz, hornblende,
231 biotite, potassium feldspar, Fe-Ti oxides (predominantly magnetite-titanomagnetite), and apatite as mineral
232 classes for the RF models (Section 3.3). For those without offline access to a full EDS environment, some
233 systems such as Oxford AZtec allow for the full export of data into text or binary formats, which can be accessed
234 with free and open-source tools (e.g., HDFView or NIST DTSA-II). Due to trace abundance (Murphy et al.,
235 1998), other minerals present in the samples like epidote and titanite lacked an adequate number of trainable
236 examples, so were neglected or combined with an associated mineral, Fe-Ti, respectively. For reference, the
237 mean abundance of apatite, the lowest abundance mineral we trained, was ~0.1%. We recommend that minerals
238 present at abundances lower than this be omitted or combined with the understanding that overall accuracy is
239 most likely being negatively impacted in a minor way.

240

241 **3.3 Smoothing and virtualization of the elemental intensity rasters**

242 We smoothed each elemental intensity raster with a 7-pixel radius circular mean filter using SAGA's Simple
243 Filter tool to eliminate noise in the EDS data. We chose this filter size because it optimized the accuracy
244 calculated during the training and validation of the RF model. We test the sensitivity of this choice in Section 4.3.
245 We then used the GDAL gdalbuildvrt command within QGIS to group the smoothed elemental intensity rasters
246 into a virtual raster dataset, in which each elemental raster is represented as a separate band. A virtual raster is a
247 container for multiple rasters that encodes metadata such as file locations and other attributes in extended markup
248 language (XML) (McInerney and Kempeneers, 2014). Opening and processing virtual raster datasets requires
249 less computer resources as the underlying rasters are only accessed when required.

250

251 **3.4 Training random forest models for mineral classification**

252 Before a RF model can be tasked with assigning a mineral class to every pixel in an entire thin section, it must
253 first be trained upon the minerals in the thin section. On each of the virtual rasters for the 14 thin sections, we
254 selected an area encompassing less than ~15% of the total thin-section sample area within which we trained the
255 model. We selected training areas that represented all minerals as well as possible, so that each mineral would

256 receive an adequate amount of training data for each mineral. Selecting a small training area in the thin section is
257 useful because it enables users to test the accuracy of the trained model on other areas of the thin section, if
258 desired. This is not a necessary step in the method, but in Section 4 we show how such accuracy tests can be done
259 on other portions of the thin sections.

260

261 For each mineral within the training area, we manually generated hundreds of circular polygons upon the virtual
262 raster using the knowledge gained previously from examining the EDS spectra (Fig. 1). A single training polygon
263 within the training area collects all pixel values contained within it from each elemental intensity raster
264 composing the virtual raster. Labelling this polygon as a single mineral, effectively labels every pixel value
265 contained within it as that mineral. We note that during this training step, the user should take care not to
266 misidentify or neglect training upon abundant minerals, which could have a detrimental effect on the
267 classification accuracy. To prevent this outcome, we used all available elemental rasters to verify that training
268 polygons were within the bounds of the identified mineral. For a few thin sections, multiple subareas composed
269 the training area to incorporate enough data on less abundant minerals like apatite. Because each training polygon
270 encompassed pixel-level data for all bands from the virtual raster, the training datasets were large ($>10^5$ pixel-
271 level samples for each thin section). Hundreds to thousands of pixel-level training samples per class are generally
272 considered sufficient for RF models (Cutler et al., 2012). Training samples per mineral were highly unbalanced
273 (i.e., some minerals covered many more pixels than others) due to the high abundances of quartz and plagioclase
274 relative to those of minor mineral like apatite. Orfeo Toolbox handles this potential problem automatically by
275 randomly selecting samples at a rate relative to the size of the smallest class, ensuring that the minority classes
276 like apatite have an equal probability of being drawn into a sample subset used to construct an individual decision
277 tree.

278

279 Using the training data obtained from the virtual raster for each thin section, we trained RF image classification
280 models using the TrainImagesClassifier function in Orfeo Toolbox. In this function, users must select
281 hyperparameter values for the RF model, which are tuneable parameters that control model behaviour. In
282 machine learning, hyperparameters define the general behaviour of a model, and are distinct from model
283 parameters, which are learned through training. For more details about RF machine learning models
284 hyperparameters, see the review in Probst et al. (2019). We used the default hyperparameter values pre-selected
285 in Orfeo Toolbox (Table 1) for the models employed for our final predicted mineral maps.

286

287 A measure of model accuracy is automatically calculated by the TrainImagesClassifier function at this step using
 288 unseen training data, which can be useful to examine before proceeding as to ensure that the RF model is
 289 operating correctly. The accuracy metric we focus on in this study is the F1 score (Equation 3), which is the
 290 harmonic mean of the precision metric (Equation 1) and the recall metric (Equation 2). This is a useful measure
 291 of the accuracy of RF-predicted minerals because it penalizes false positives and false negatives while rewarding
 292 true positives and neglecting true negatives (Chinchor and Sundheim, 1993), which can be very plentiful for low
 293 abundance minerals.

$$Precision = \frac{True\ positives}{True\ positives + False\ positives} \quad (1)$$

$$Recall = \frac{True\ positives}{True\ positives + False\ negatives} \quad (2)$$

$$F1\ score = \frac{2(Precision)(Recall)}{Precision + Recall} \quad (3)$$

297 In the application of Equations 1-3 to mineral maps, a true positive is defined as pixel-level agreement on the
 298 presence of a given mineral between the model prediction and unused training data, which the algorithm holds
 299 out from training for the purpose of calculating metrics such as the F1 score. Similarly, a true negative is
 300 agreement on the absence of a given mineral class. False positives and false negatives are disagreements on the
 301 presence and absence of a given mineral class, respectively. Application of the default hyperparameters to our
 302 samples yielded very high F1 scores (~0.99). This gave us confidence that the predicted mineral maps generated
 303 using the default hyperparameters were near optimal for comparison with manually delineated test maps
 304 (described in Section 4.1).

Table 1. Default hyperparameter values for Orfeo Toolbox RF machine learning model and typical values according to Probst et al. (2019).

Parameter name	Orfeo Toolbox value	Typical value(s)
Maximum number of trees in the forest	100	500-1000
Maximum depth of tree	5	N/A
Size of the randomly selected subset of features at each tree node	(number of features) ^{1/2}	(number of features) ^{1/2}

307

308

309 We applied each trained model to its corresponding virtual raster to predict a single mineral class at each pixel,
310 except in the case of ensemble voting ties, in which case no mineral class was assigned to that pixel. This resulted
311 in mineral maps at the same resolution as the virtual rasters ($\sim 4 \mu\text{m}$).

312

313 3.5 Using the random forest models to generate mineral maps

314 In our application of the trained RF models to our thin sections, the models calculated the entire thin-section scale
315 mineral maps in a under a minute using a desktop computer (4 GHz processor; 64 GB memory). Figure 1 shows
316 an example of one of these mineral maps.

317

318 After a thin section's mineral map has been generated, it is trivial to calculate the abundance of each mineral by
319 counting pixels. Figure 2 shows the abundance of each mineral across all 14 samples with the error given by the
320 mean F1 scores of the minerals. It also reveals relatively little variation in each mineral's abundance among the
321 14 samples, which is consistent with previous observations of the Rio Blanco tonalite. The RF-predicted mineral
322 abundances compare well with those measured from modal analysis via point counting on BSE imagery (Buss et
323 al., 2008) and via quantitative XRD (Ferrier et al., 2010). Buss et al. (2008) measured average areal abundances
324 of 19.9% and 49.3% for quartz and plagioclase, respectively, comparable to the RF-predicted average abundances
325 of $22.8 \pm 1.0\%$ and $55.8 \pm 2.3\%$ (\pm error from mean F1 scores) on our 14 thin sections. The combined abundance
326 of hornblende and biotite ('Fe-silicates') measured by Buss et al. (2008) was 24%, which is close to the
327 maximum RF-predicted abundance of 'Fe-silicates' among our 14 samples ($25.0 \pm 1.5\%$). Using common values
328 for molar masses (M mol^{-1}) and densities (M L^{-3}), the XRD-based abundances (converted to areal abundance)
329 from Ferrier et al. (2010) for quartz, plagioclase, and hornblende were 24%, 62%, and 14%, respectively, while
330 the RF-predicted mineral maps yielded $22.8 \pm 1.0\%$, $55.8 \pm 2.3\%$, and $10.4 \pm 0.7\%$, respectively. When quartz,
331 plagioclase, and alkali feldspar abundances are normalized for usage with a Quartz-Alkali Feldspar-Plagioclase-
332 Feldspathoid diagram (Le Maitre, 2002), the RF-predicted abundances for each mineral demonstrated that all thin
333 sections can be classified as tonalite, matching the name of the lithology.

334

335

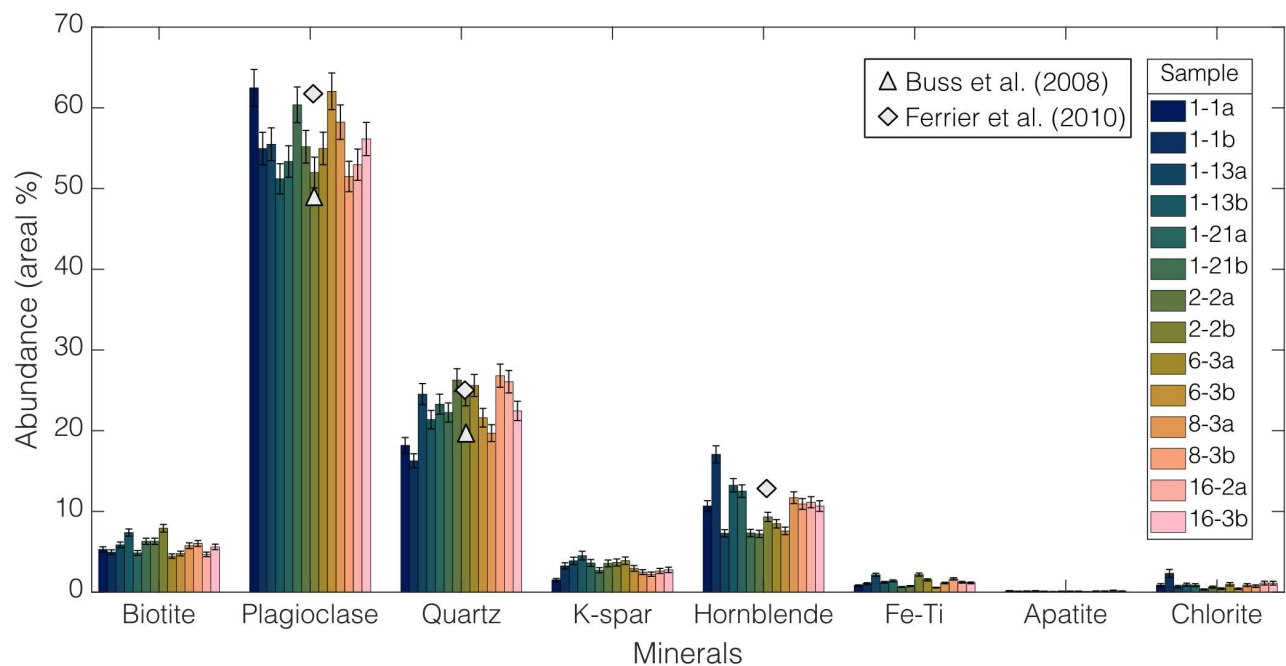


Figure 2. Areal abundance for all 14 samples of the Rio Blanco tonalite. Error bars stem from mean F1 scores for each individual minerals from test map comparisons (see Section 4.1). Data from the analyses of the Rio Blanco tonalite in Buss et al. (2008) and Ferrier et al. (2010) included for reference.

4. Discussion: Accuracy of random forest-predicted mineral maps and sensitivity analyses

4.1 Accuracy of random forest-predicted mineral maps

Before applying the trained RF models to the full thin sections, we manually mapped the mineralogy of a small section for three representative samples (6-3a, 16-2a, and 1-13a) to assess the accuracy of the model-generated mineral maps. We refer to these manually delineated mineral maps as “test maps”. These test maps were manually delineated as vector polygons for all mineral classes using the elemental intensity rasters for guidance. For example, when mapping a grain of potassium feldspar, we determined the boundaries of the grain with filtered and unfiltered rasters of K as well as combined intensity rasters of multiple elements. We consider these maps to be ‘ground truth’ data, which are never perfect representations of reality (Foody, 2024), but, nonetheless, may serve to compare the performance of this method to the extremely slow process of manually mapping grain boundaries. We then rasterized the manually-delineated vector maps, which resulted in the classification of every pixel within the test maps as one of the eight minerals. The test maps averaged over 1 million pixels in size.

350

351 We compared the same section of the predicted mineral maps to the test maps using a frequency-weighted F1
352 score (Equation 4) to gauge the average accuracy for all mineral classes. To calculate a frequency-weighted F1
353 score, the F1 score for the i^{th} class ($F1\ score_i$) is weighted by the class frequency (w_i), which is the proportion of
354 pixels of class i to the total number of pixels in the test map. Here, N is the number of mineral classes.

355

$$Frequency - weighted\ F1\ score = \sum_{i=1}^N w_i F1\ score_i \quad (4)$$

356

357 We clipped the portion of the predicted mineral map overlapping the test map from the full map for each of the
358 three thin sections with a test map. From these two rasters, we calculated the frequency-weighted F1 score.

359

360 The RF-generated mineral maps in Section 3 exhibited high accuracy. For the three thin sections that were
361 mapped both manually and by the RF-based method in Section 2, the mean frequency-weighted F1 score among
362 the three thin sections was 0.948 ± 0.002 , meaning that nearly 95% of the pixels in the RF-predicted maps agreed
363 with those in the manually delineated maps (Table 2). The accuracy varied among minerals. The four most
364 abundant minerals (plagioclase, quartz, hornblende, and biotite) all have mean F1 scores of 0.94 to 0.96, while
365 apatite, the least abundant mineral, had the lowest mean F1 score of 0.72. A closer look at the precision and recall
366 metrics for apatite show that mean recall scores (0.62) were lower than mean precision (0.91). This indicates that
367 the models correctly predicted apatite when attempted but the models often neglected to predict apatite. Because
368 apatite is rare and appears as small inclusions in our samples, less training data was collected for it than for other
369 minerals in each sample. This can result in class imbalances in training data, which, for rare mineral classes (in
370 our case, apatite), can produce scenarios in which the model does not try to predict the mineral class, as the
371 diversity of training data for rare classes (in our case, apatite) remains relatively low (He and Garcia, 2009).
372 Abundance and the mean F1 score were not always linked; for example, Fe-Ti oxides were low in abundance
373 ($\sim 1\%$) but registered a mean F1 score of 0.91.

374

375 Figure 3 shows an example of an RF-predicted mineral map with misclassified pixels shown in red. This
376 illustrates a key point: the accuracy of the RF-predicted mineral maps is not spatially uniform. Most pixels that
377 diverge from manual classification occur at grain boundaries where elemental compositions shift abruptly in

378 space. By contrast, in mineral grain interiors, divergent pixels are far less common. This indicates that the
379 accuracy of RF-predicted mineralogy in grain interiors is higher than the F1 scores in Table 2.

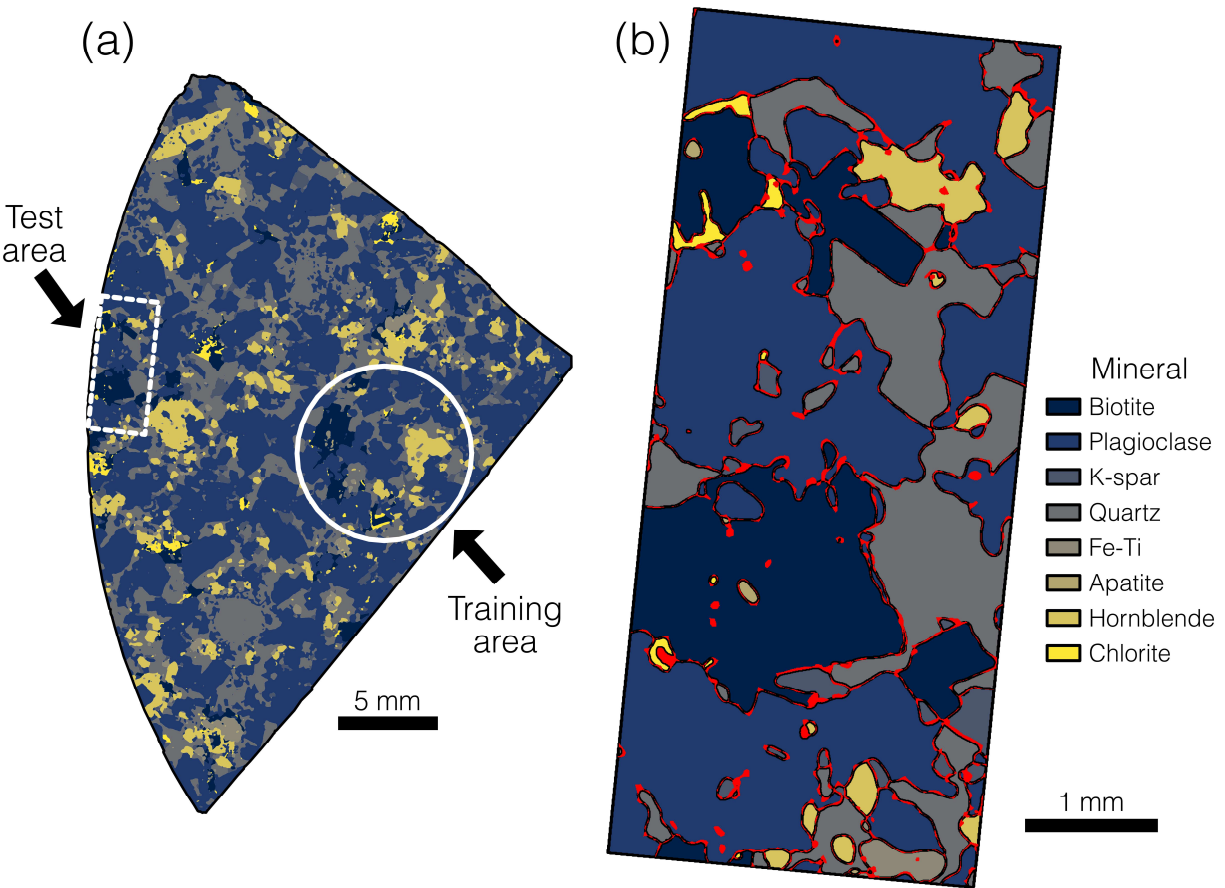


Figure 3. (a) Predicted mineral map for sample 6-3a, showing the location of the manually delineated test map, which we used to check accuracy. (b) Predicted mineral map for the test area. Red color signifies where pixels in the predicted map diverge from the manually delineated test map. This shows that most divergent pixels are at mineral grain boundaries.

380
381 A combined confusion matrix for pixel-level comparisons from every test and predicted map showed the most
382 common divergent classification was chlorite for biotite. This is likely because biotite and chlorite have similar
383 elemental compositions and because they often share a grain boundary (chlorite is a product of hydrothermal
384 alteration of biotite), which means they are more prone to disagreement along grain boundaries. Among the major

minerals, our models divergently classified potassium feldspar as plagioclase feldspar most often, likely because many potassium feldspar grains in the Rio Blanco tonalite contain small amounts of Na, like plagioclase.

Figure 4 shows close agreement between the RF-predicted abundance and the manually mapped abundance in the test areas, with a mean difference for a given mineral of $0.45 \pm 0.02\%$ across the three test maps. So, although some predicted pixels were misaligned spatially, the RF-predicted mineral abundances agree well with manual estimates derived from the test maps.

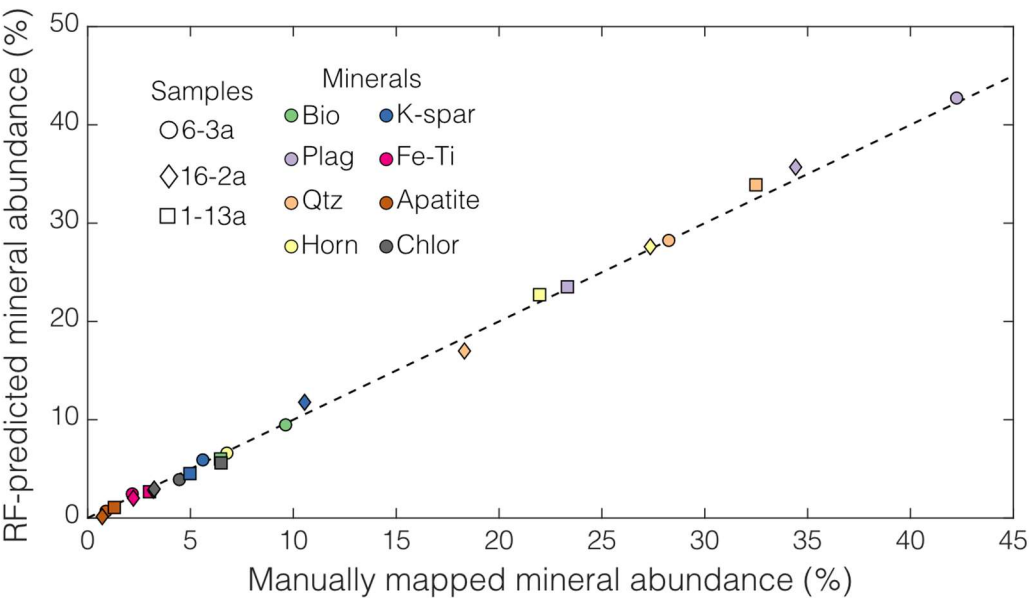


Figure 4. RF model-predicted mineral abundance vs. manually mapped mineral abundance in the test areas of the three samples with test maps. The dashed line is a 1:1 line. Although there was some spatial mismatch around the edge of mineral grains (e.g., Fig. 3), the RF-predicted modal abundances agree well with abundances inferred from manual mapping in the test areas.

392

393

Table 2. Mean F1 scores (accuracy metric) for mineral classes among the three test maps (Fig. 4), based on comparison of automated mineralogy maps to manually delineated mineralogy maps.

Mineral	Mean F1 score
---------	---------------

All classes (frequency-weighted)	0.95
Plagioclase feldspar	0.96
Quartz	0.94
Hornblende	0.94
Biotite	0.94
Potassium feldspar	0.88
Fe-Ti oxides	0.91
Chlorite	0.79
Apatite	0.72

4.2 Sensitivity of mineral maps to random forest hyperparameters and input features

In our application of the method in Section 2 to the 14 samples in Section 3, we used a set of default values for three RF hyperparameters: maximum tree depth, number of trees, and minimum sample size per node. Reviews of hyperparameter tuning on RF models have shown that the number of trees and the minimum number of classes per node can have a large effect on classification accuracy (Probst et al., 2019). In this section we gauge the sensitivity of our results to hyperparameter values and input features.

Orfeo Toolbox does not contain a facility for hyperparameter tuning in QGIS, so we developed a workflow to undertake our own hyperparameter optimization outside of QGIS in Python. This is not a necessary step in the method, but we have included this code in the Supplement for users who wish to conduct their own hyperparameter optimization. We began by converting the smoothed elemental intensity image data in the three training areas within the manually delineated test maps into NumPy arrays (Harris et al., 2020) using a combination of three Python libraries: rasterio (Gillies et al., 2019), geopandas (Jordahl et al., 2020), and shapely (Gillies et al., 2022). We then used the implementation of the RF classifier from the machine-learning package scikit-learn (Pedregosa et al., 2011) for both hyperparameter optimization using a randomized five-fold cross validation (Breiman and Spector, 1992) and derivation of feature importance using permutation testing (Breiman, 2001). Through these operations we seek to find optimal hyperparameters and test the importance of input features (here, elements), respectively.

We used the scikit-learn RandomizedGridCV function to systematically test the sensitivity of the output mineral maps to the RF hyperparameter values. To do this, we trained 100 unique RF models across a range of maximum

tree depth (1-100), number of trees (10-2000), and minimum sample size per node (5-25). These hyperparameters are common between the Orfeo Toolbox and scikit-learn implementations of the RF classifier. We used five-fold cross-validation, in which each randomly selected set of hyperparameters is used to train the same model five times while sampling different portions of the training data (Breiman and Spector, 1992). We report the best fit parameters and resultant accuracy in terms of the frequency-weighted F1 score upon comparison to the test maps using these optimized parameters.

Orfeo Toolbox has not yet incorporated a capacity to derive feature importance scores. Feature importance in RF classification is calculated by permutation testing, which is the extent to which an accuracy metric declines if a single input feature's unused training data is randomly altered during the training process and validation process (Breiman, 2001; Guo et al., 2011). We used the sci-kit learn function `permutation_importance` to assess importance using the frequency-weighted F1 score. We report the feature importance for the three samples with manually delineated test maps and discuss their implications.

Tuning the hyperparameters in scikit-learn showed that both a higher maximum tree depth and number of trees may be optimal for our RF models, while the minimum sample for splitting was more variable (Table 3). Using these optimized RF hyperparameters within Orfeo Toolbox yielded a mean frequency-weighted F1 score of 0.95 when comparing the three samples with manually delineated test maps, which is the same F1 score realized by using the default hyperparameters. As the two implementations of the RF classifier are somewhat different in terms of available hyperparameters, the comparison is imperfect but does provide a check to see if the default hyperparameters could be improved upon. That an optimized set of hyperparameters delivered very little to no increase in accuracy is unsurprising as RF models are known to perform well with little to no tuning if reasonable hyperparameter values are initially used (Maxwell et al., 2018). Unless low F1 scores are realized during Step 4, it is our recommendation that the default RF hyperparameters in Orfeo Toolbox be used.

Table 3. Optimal RF hyperparameters from five-fold cross validation performed using sci-kit learn.

Sample	Maximum tree depth	Number of trees	Minimum sample for split
--------	-----------------------	--------------------	-----------------------------

1-13a	73	1685	25
6-3a	94	1371	5
16-2a	73	1581	5

442

443

444 Feature importance, as determined through permutation testing, showed that both K and Mg were the most
445 important features for our scikit-learn trained models with mean decreases in accuracy based on frequency-
446 weighted F1 scores derived from the training and validation process on unused data of 0.29 for both elements
447 (Fig. 5). Ti was relatively unimportant with a very small, slightly positive value, implying it could be omitted.
448 Although Ti is present within biotite and Fe-Ti oxides in our samples, Ti showed little to no decrease in mean
449 accuracy as both biotite and Fe-Ti oxides can be classified using other elements. We tested whether our feature
450 importance scores were pertinent to models in Orfeo Toolbox by leaving out, in turn, K, Mg, and Ti during
451 training and validation process. Excluding K decreased mean F1 scores due to the degradation of potassium
452 feldspar, biotite, and chlorite accuracy. In contrast, omitting Mg did not decrease F1 scores, showing that a
453 feature importance score does not directly translate to decreased model accuracy upon omission (Cutler et al.,
454 2011). Leaving out Ti had little effect on F1 scores. If a user of our method is unsure whether an element could
455 be a truly important feature, omitting an important element from the training process by creating virtual rasters
456 without that element should yield a notable degradation in training F1 scores.

457

458

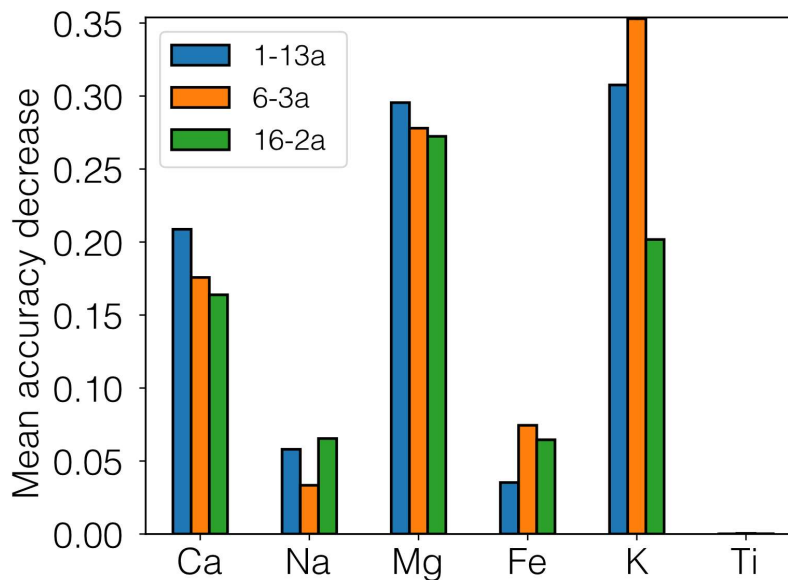


Figure 5. Feature importance from scikit-learn using permutation testing for all six input elements for the three samples with test maps. Mean accuracy decrease is the change in the F1 score due to randomly changing feature data in the unused portion of the training data during the validation process. In Orfeo Toolbox, training models that omitted K degraded F1 scores while those that omitted Mg yielded little change, indicating that feature importance score does not always directly map onto model accuracy and that some experimentation with input features (elements) during the training phase is warranted.

459

460 **4.3 Sensitivity of mineral maps to filter sizes**

461 In our application of this method to our samples, we applied a circular, 7-pixel radius mean filter to the EDS-
 462 generated elemental intensity rasters (Step 2 in Section 2), and we applied a circular, 10-pixel radius majority
 463 filter to the output mineral maps (Step 6). To quantify the sensitivity of the output mineral maps to these “hidden”
 464 parameters, we generated a series of RF models across a range of mean filter radii for the elemental intensity
 465 rasters (no filter, 2, 5, 7, 10, and 20 pixels) and a range of majority filter radii (no filter, 2, 5, 7, 10, and 20 pixels).
 466 For the three thin sections with manually delineated mineral maps, we calculated the frequency-weighted F1
 467 score of the entire thin section by comparing each of the RF-predicted mineral maps to the manually delineated
 468 test maps.

469

470 Figure 6 reveals that both the mean filter and the majority filter affect the accuracy of the predicted mineral maps.
471 The largest impact on the accuracy, as measured by F1 score, was in the application of any mean filter at all to
472 the input elemental intensity rasters. The left panel in Fig. 6 shows that applying no mean filter to the elemental
473 intensity rasters produced low F1 scores (0.52-0.69) for all models and all samples, regardless of the size of the
474 majority filter. Accuracy increased with mean filter radius up to 5 and 7 pixels, which yielded high F1 scores at
475 all majority filter sizes (0.91-0.96) due to the elimination of spurious inclusions within larger mineral grains
476 (middle panels in Fig. 6). Beyond that size, accuracy decreased slightly with higher mean filter radius, with lower
477 F1 scores at radii of 10 pixels (F1 scores of 0.90-0.95) and 20 pixels (0.87-0.89). This implies an intermediate
478 optimal mean filter radius of 5-7 pixels for these samples.
479
480 Accuracy was sensitive to the size of the majority filter, particularly for models that applied no mean filter or a
481 small (2-pixel radius) mean filter to the input elemental intensity rasters (Fig. 6). For the models that applied a
482 mean filter of any size, accuracy was lower at small majority filter radii (0 or 2 pixels) and large radii (20 pixels)
483 than at intermediate majority filter radii (5-10 pixels). At the largest radii, the RF-predicted mineral grains begin
484 to lose shape, becoming more circular. Thus, accuracy was maximized at intermediate majority filter radii of 5-7
485 pixels, just as it was at intermediate mean filter radii. Excluding plagioclase and quartz (which generally do not
486 occur as isolated grains), the three samples with test maps (6-3a, 1-13a, and 16-2a) have a median grain area of
487 $\sim 0.005 \text{ mm}^2$ ($n = 5188$ mineral grains across all three samples) while the 5-7-pixel radii filters have areas of
488 $\sim 0.001 \text{ mm}^2$ and $\sim 0.002 \text{ mm}^2$, respectively. These optimal sizes most likely result from a mix of the initial EDS
489 pixel resolution and data quality and the types and sizes of minerals in the thin section (Lanari et al., 2014;
490 Ortolano et al., 2018), so we recommend that users experiment to find the optimum filter sizes for their samples.
491
492

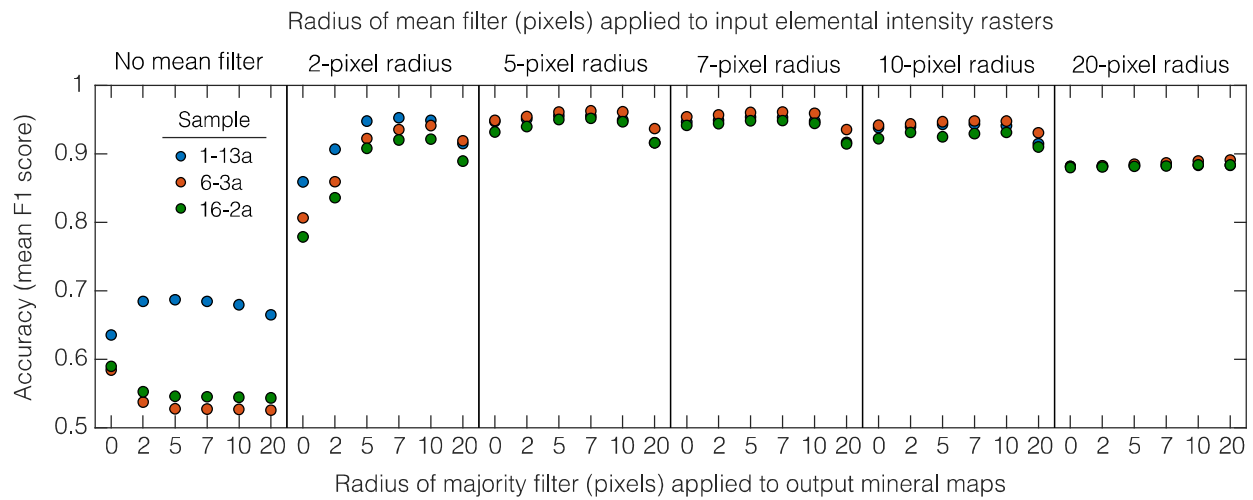


Figure 6. Accuracy of the output mineral maps (as quantified by frequency-weighted mean F1 scores) for combinations of mean filter and majority filter sizes for the three samples with test maps. Each section is a single mean filter size. The most accurate mineral maps (i.e., those with the highest F1 scores) were generated using a 5- or 7-pixel radius mean filter combined with a 5- or 7-pixel radius majority filter.

493

494 **5 Discussion: Advantages, utility, and limitations**

495

496 **5.1 Advantages of this open-source automated mineralogy method**

497 Situating our workflow in a free and open-source GIS environment confers several practical benefits. Both Orfeo
 498 Toolbox and QGIS are frequently updated with source code that can be examined and modified, unlike many
 499 proprietary hardware/software systems (Keulen et al., 2020). Orfeo Toolbox and QGIS each have extensive
 500 documentation and user forums monitored by the developers, which can aid in addressing user issues (Raza and
 501 Capretz, 2015). Incorporating open-source software into scientific methods fosters transparency and
 502 reproducibility as the software is widely accessible and more easily scrutinized (Ramachandran et al., 2021). As
 503 both Orfeo Toolbox and QGIS are ongoing efforts with active contributing communities, our no-code workflow
 504 is tied to software that is not likely to fall into disrepair or unavailability, unlike much open-source scientific
 505 software (Coelho et al., 2020). Furthermore, both Orfeo Toolbox and QGIS are available for all major operating
 506 systems, Windows, macOS (Intel), and Linux, so this factor does not limit accessibility. Orfeo Toolbox will
 507 likely continue to incorporate new state-of-the-art machine-learning algorithms. For example, Orfeo Toolbox has

508 recently been unofficially extended to utilize the Google TensorFlow library (Abadi et al., 2016) to perform deep-
509 learning tasks on remote sensing imagery (Cresson, 2018, 2022). There are also efforts to develop open-source
510 scanning electron microscope systems and attendant software such as the NanoMi project (Malac et al., 2022).
511 All of this means that automated mineralogy methods are likely to become more popular and accessible.

512

513 We expect that a broad range of geoscientists will be capable of using this GIS-based method, since many
514 geoscience undergraduate programs incorporate GIS into courses (Marra et al., 2017). It requires no
515 programming skill to obtain mineral maps, thereby eliminating a potential barrier for use (Bowlick et al., 2016).
516 Since the workflow takes place within a GIS environment, the input elemental intensity rasters could easily be
517 processed in other ways besides the mean smoothing filter that we applied here, such as edge-detection filtering
518 or elemental intensity ratioing. Creation of optimal input features, so-called feature engineering, is fostered by the
519 many QGIS frontends that interface with SAGA GIS and GDAL raster manipulation programs. Our method does
520 not require a corresponding plugin for Orfeo Toolbox/QGIS, but much of it could be automated from the Orfeo
521 Toolbox/QGIS Python API or as QGIS console commands, if desired. Input parameters for image filters and
522 hyperparameters for the RF models can be saved as JavaScript Object Notation (JSON) files, which can be
523 loaded in later, overcoming some of the reproducibility issues inherent in workflows using graphical user
524 interfaces (Brundson, 2016).

525

526 **5.2 Illustration of the utility of random forest-generated mineral maps**

527 There are many potential uses for thin section-scale mineral maps once they have been generated. Converting the
528 mineral maps into vector form allows for the calculation of derived parameters such as median grain area for
529 minerals that occur as single grains (e.g., biotite), distance between grains of a mineral, and the types of minerals
530 surrounding a grain or grains in the case of abundant, connected minerals like plagioclase and quartz. This type of
531 data is normally generated by proprietary automated mineralogy systems but could aid in geoscience disciplines
532 beyond ore geology or petroleum geology (Han et al., 2022). An illustrative example is in the analysis of grain-
533 scale properties of biotite. This is of wide interest because oxidation of ferrous Fe in biotite drives expansion of
534 biotite grains, which generates stresses in the surrounding rock that may be large enough to fracture the rock
535 (Fletcher et al., 2006; Goodfellow et al., 2016; Goodfellow and Hilley, 2022). To the extent that biotite expansion
536 promotes generation of regolith from bedrock, it may even influence the km-scale evolution of mountainous
537 topography (Wahrhaftig, 1965; Xu et al., 2022). In granitic rocks, numerical modelling has shown that biotite
538 abundance influences the accrual of microscale damage (Shen et al., 2019) and weathering profile development is

539 partially guided by biotite crystal size (Goodfellow and Hilley, 2022). These are two properties that can be
540 directly measured in our thin section-scale mineral maps.

541

542 To obtain such mineral maps in some previous studies, researchers have often engaged in manual or semi-
543 automated characterizations of sample mineral properties (Buss et al., 2008; Ündül, 2016). These workflows are
544 often tailored for a single study (e.g., Goodfellow et al., 2016). Methods that are based on generalizable
545 workflows involving automated mineralogy methods such as the one presented in this study could enhance
546 comparability between studies. Since we converted the predicted mineral maps into a vector (polygon) form
547 within QGIS, we could use built-in functions to gather large amounts of data on grain neighbours or perform
548 grain size measurements. As we discuss in Section 5.3, classified biotite ‘grains’ may contain multiple bordering
549 crystals of the same mineral as our EDS input data, and the resultant classification cannot differentiate boundaries
550 by elements alone (Lanari et al., 2014). As biotites are relatively isolated from each other in our thin sections,
551 these measurements serve as a reasonable indicator of true biotite properties. For example, the 20 largest biotite
552 grains in samples 1-1a and 6-3b comprise 80% and 94% of the total biotite area, respectively (Fig. 7a-b). The
553 median grain area of these 20 biotite grains in sample 1-1a is 0.60 mm^2 , several times larger than that in sample
554 6-3b (0.19 mm^2 ; Fig. 7c).

555

556 We can also use raster morphology operations on the mineral maps to measure distances between classified
557 minerals. In analog and numerical experiments that impose stress on granitic rocks (Tapponier and Brace, 1976;
558 Li et al., 2003; Mahboudi et al., 2012), biotite grains can act as preferential origination points for microfractures,
559 but biotite can also arrest propagation of microfractures arising from neighboring grains. Thus, the distance
560 between biotite grains may be an important, yet rarely measured property. In the example of the two samples in
561 Fig. 7, biotite grains have similar median distances from one another but different probability distributions of
562 distances between biotite grains, particularly in the long tail of the distributions at larger distances (Fig. 7e). We
563 can also extract the composition of neighbouring grains surrounding biotite (Fig. 7f), which reveal that chlorite is
564 much more abundant near biotite relative to the rest of the thin section. Data like these can be useful for those
565 studying the impacts of different grain-grain contacts on stress response during rock mechanics experiments (e.g.,
566 Aligholi et al., 2019), which has shown that some mineral interactions can have an outsized influence on the
567 development of fractures and failure. In sum, the data in Fig. 7 illustrate the potential power of RF-generated
568 mineral maps to improve quantitative in-situ investigations of biotite weathering (Behrens et al., 2021) and form
569 the basis for more realistic models of biotite-driven rock damage (Shen et al., 2019).

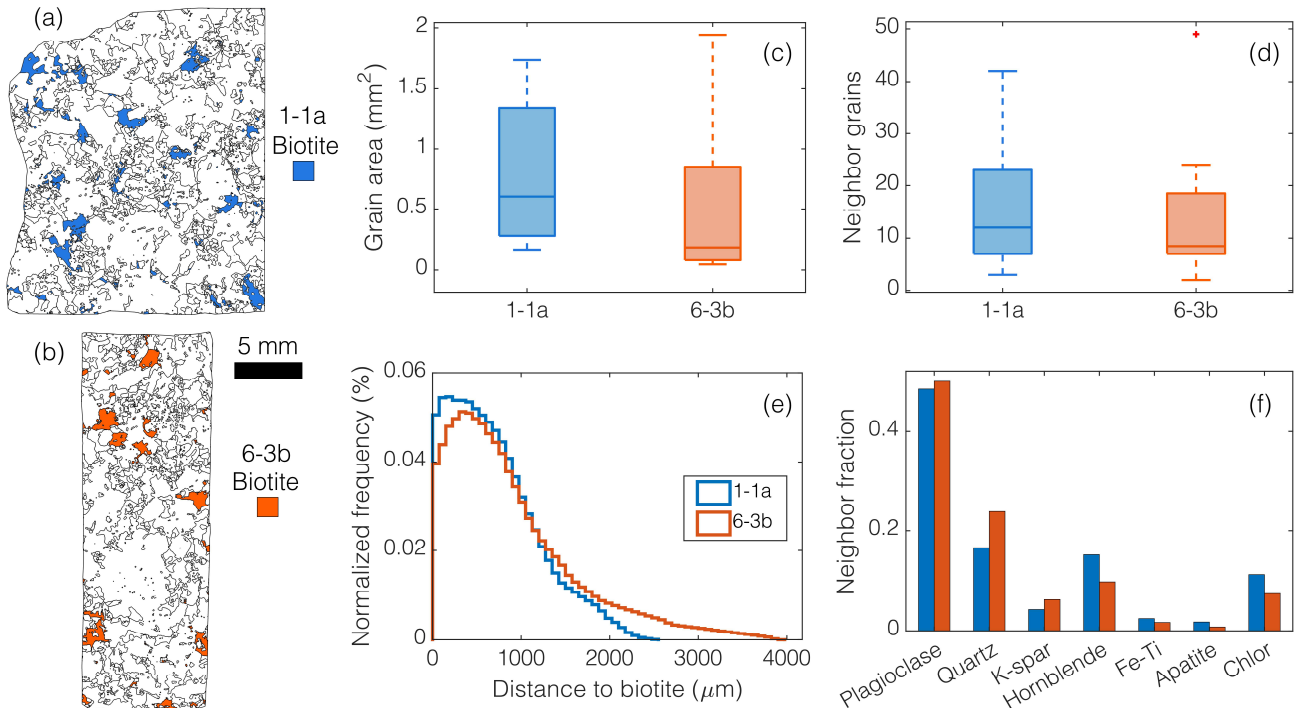


Figure 7. Example of quantities that can be obtained from mineral maps generated by the automated method in this study. (a-b). Colours highlight biotite grains identified in the RF-generated mineral maps in thin sections 1-1a (blue) and 6-3b (orange). (c-f). Biotite properties extracted from predicted maps for the 20 largest biotite grains in each sample. These data could help inform numerical models of microcrack generation and allow for quantitative comparisons between different samples or lithologies (e.g., Shen et al., 2019). (c) Boxplot of biotite grain area (mm²) for the 20 largest biotite grains for both samples. (d) Boxplot of number of grains surrounding the largest 20 biotite grains. (e) Normalized frequency distribution of distances between biotite pixels (not including those inside a biotite grain). (f) Composition of neighbours as a fraction of perimeter.

571

572

573 5.3 Limitations

574 Our method's greatest asset is that it can generate thin section-scale mineral maps without requiring the use of
575 propriety software or a background in programming. Its most important limitation is that it is most accurate if the
576 user trains a RF model for every thin section sample. Using a RF model that was trained on one sample to predict
577 mineral maps for another sample can yield mineral maps that accurately map minerals in some areas but

578 inaccurately in others. For example, when we applied a RF model that was trained on sample 16-2a to sample 6-
579 3a, apatite abundance was overpredicted by a factor of 5 possibly due to 6-3a having some highly calcic zones
580 within plagioclase grains. So, for the most accurate results, we recommend training each thin section separately.
581

582 A second limitation is that this method tends to be less accurate at identifying low abundance minerals. Unlike
583 some proprietary automated mineralogy software systems, our method does not use predefined EDS spectra to
584 identify minerals. Instead, our method trains RF models on the samples themselves, which means that each
585 mineral of interest must be abundant enough to properly train the RF model. The relatively low F1 scores of the
586 lower abundance minerals in our samples (Table 2) suggest that the minimum abundance required to train a RF
587 model is larger for minerals with small grain size (e.g., in the case of apatite) and a lack of compositional
588 distinction (e.g., in the case of chlorite). Minerals must be resolvable by the EDS data, so collecting EDS data
589 with a field-emission-gun SEM at higher resolution ($\sim 0.1 \mu\text{m}$) could improve mineral classification in rocks with
590 finer grain size distributions (Han et al., 2022).

591

592 A final limitation is that mineral grains that border mineral grains of the same mineral appear to the RF model as
593 regions of the same mineral and, hence, can be classified as a single mineral grain, rather than two grains. This is
594 a common issue shared with other automated mineralogy methods (Lanari et al., 2014; Hrtska et al., 2019), and it
595 can affect inferred probability distributions of mineral grain size of those mineral if not properly accounted for.

596

597 **6. Conclusions**

598 The main contribution of this study is a new automated method for obtaining mineral maps from EDS scans of
599 rock thin sections. This method is implemented within a free and open-source GIS application, uses free and
600 open-source plugins for RF image classification, and requires no programming. To demonstrate the utility of this
601 method, we trained RF models on EDS scans of 14 thin-section samples of a well-studied, plutonic igneous rock.
602 The resulting model-predicted mineral maps compare well with manually delineated mineralogy maps, with 95%
603 of pixels on the mineral maps predicted correctly. With regards to the most abundant minerals in the Rio Blanco
604 tonalite, plagioclase feldspar and quartz, the models attained 96% and 94% accuracy, respectively.

605

606 We utilized scikit-learn's implementation of the RF classifier to search for optimal RF hyperparameters and to
607 test input feature (element) importance. We saw no increase in accuracy using optimal hyperparameters found in
608 scikit-learn when used within Orfeo Toolbox, so we recommend using the default hyperparameters. We did see

609 that an important input feature, K, did lower accuracy when not included in Orfeo Toolbox-based models, so
610 some level of experimentation with input features during the training step is warranted. We also tested to see if
611 our pre- and post-processing steps had a large influence on accuracy by using different sizes of mean and
612 majority filters. An absence of filtering and excessively large filters led to lower accuracy while filters in the
613 range of 5-10 pixels for both mean and majority filters led to higher accuracy.

614

615 Situating the workflow within a free and open-source GIS environment confers distinct advantages. Open source
616 extends benefits such as source code availability, extensive documentation, and accessibility. Moreover, as the
617 workflow is within a GIS environment, the application is likely to be familiar to a range of geoscientists. Also, all
618 the available tools (e.g., different types of image filters) within the GIS allow for easy input feature
619 experimentation. The mineral maps from our method proved highly accurate when compared to manually-
620 delineated maps, and estimates of mineral abundance compared well to previous estimates from the literature for
621 our sample lithology. Many of the measured quantities produced by proprietary automated mineralogy systems
622 are obtainable once predicted mineral maps are converted to vector datasets. These measurements, such as
623 median grain size and amount of grain neighbours, can be useful to researchers studying microscale damage
624 processes that arise through rock weathering or rock mechanics experiments. We hope that this method will be
625 useful for researchers who wish to obtain rapid, automated mineralogy maps of thin sections.

626

627 **Code and Data availability**

628 The manuscript supplement containing the code for analysis and visualizations is available through a Zenodo
629 repository (<https://zenodo.org/doi/10.5281/zenodo.10912627>; Reed et al., 2024). The supplement also contains
630 data (smoothed elemental intensity rasters, training polygons, and test maps) for the three thin sections with
631 manually delineated test maps.

632

633 **Author contribution**

634 **Miles Reed**: conceptualization, formal analysis, methodology, software, visualization, and writing (original draft
635 and preparation); **Ken Ferrier**: funding acquisition, supervision, visualization, and writing (review and editing);
636 **William Nachlas**: resources and writing (review and editing); **Bil Schneider**: investigation and writing (review
637 and editing); **Chloe Arson**: funding acquisition and writing (review and editing); **Tingting Xu**: writing (review
638 and editing); **Xianda Shen**: writing (review and editing); **Nicole West**: funding acquisition and writing (review
639 and editing).

640

641 **Competing interests**

642 The authors declare no competing interests.

643

644 **Acknowledgements**

645 This work was supported by NSF award EAR-1934458 and NSF award EAR-1755321.

646

647 **References**

- 648 Abadi, M., Agarwal, A., Barham, P., Brevdo, E., Chen, Z., Citro, C., ... and Zheng, X: Tensorflow: Large-scale
649 machine learning on heterogeneous distributed systems. arXiv [preprint],
650 <https://doi.org/10.48550/arXiv.1603.04467>, 16 March 2016.
- 651 Aligholi, S., Lashkaripour, G. R., and Ghafoori, M: Estimating engineering properties of igneous rocks using
652 semi-automatic petrographic analysis. Bull. Eng. Geol. Environ., 78, 2299-2314. [https://doi.org/10.1007/s10064-](https://doi.org/10.1007/s10064-018-1305-7)
653 [018-1305-7](https://doi.org/10.1007/s10064-018-1305-7), 2019.
- 654 Behrens, R., Wirth, R., and von Blanckenburg, F: Rate limitations of nano-scale weathering front advance in the
655 slow-eroding Sri Lankan Highlands, Geochim. Cosmochim. Acta, 311, 174-197,
656 <https://doi.org/10.1016/j.gca.2021.06.003>, 2021.
- 657 Berrezueta, E., Domínguez-Cuesta, M. J., and Rodríguez-Rey, Á: Semi-automated procedure of digitalization and
658 study of rock thin section porosity applying optical image analysis tools, Comput. Geosci., 124, 14-26,
659 <https://doi.org/10.1016/j.cageo.2018.12.009>, 2019.
- 660 Bjørlykke, K: Relationships between depositional environments, burial history and rock properties. Some princi-
661 pal aspects of diagenetic process in sedimentary basins, Sediment. Geol., 301, 1-14,
662 <https://doi.org/10.1016/j.sedgeo.2013.12.002>, 2014.
- 663 Blannin, R., Frenzel, M., Tuşa, L., Birtel, S., Ivăşcanu, P., Baker, T., and Gutzmer, J: Uncertainties in quantitative
664 mineralogical studies using scanning electron microscope-based image analysis, Miner. Eng., 167, 106836,
665 <https://doi.org/10.1016/j.mineng.2021.106836>, 2021.
- 666 Breiman, L: Random forests, Mach. Learn., 45, 5-32, <https://doi.org/10.1023/A:1010933404324>, 2001.
- 667 Breiman, L., and Spector, P: Submodel selection and evaluation in regression: The X-random case, Int. Stat.
668 Rev., 291-319, <https://doi.org/10.2307/1403680>, 1992.
- 669 Brocard, G., Willebring, J. K., and Scatena, F. N: Shaping of topography by topographically-controlled vegetation
670 in tropical montane rainforest, PLoS One, 18(3), e0281835, <https://doi.org/10.1371/journal.pone.0281835>, 2023.
- 671 Brunson, C: Quantitative methods I: Reproducible research and quantitative geography, Prog. Hum. Geogr.,
672 40(5), 687-696, <https://doi.org/10.1177/0309132515599625>, 2016.

673 Bürgmann, R., and Dresen, G: Rheology of the lower crust and upper mantle: Evidence from rock mechanics,
 674 geodesy, and field observations, *Annu. Rev. Earth Planet. Sci.*, 36, 531-567, <https://doi.org/10.1146/annurev.earth.36.031207.124326>, 2008.

676 Buss, H. L., Sak, P. B., Webb, S. M., and Brantley, S. L.: Weathering of the Rio Blanco quartz diorite, Luquillo
 677 Mountains, Puerto Rico: Coupling oxidation, dissolution, and fracturing, *Geochim. Cosmochim. Acta*, 72(18),
 678 4488-4507, <https://doi.org/10.1016/j.gca.2008.06.020>, 2008.

679 Callahan, R. P., Riebe, C. S., Sklar, L. S., Pasquet, S., Ferrier, K. L., Hahm, W. J., ... and Holbrook, W. S.: Forest
 680 vulnerability to drought controlled by bedrock composition, *Nat. Geosci.*, 15(9), 714-719,
 681 <https://doi.org/10.1038/s41561-022-01012-2>, 2022.

682 Callister, W. D., and Rethwisch, D. G.: Callister's Materials Science and Engineering, Global Edition, 10th Edi-
 683 tion, John Wiley & Sons, ISBN 978-1-119-45520-2, 2019.

684 Chinchor, N., and Sundheim, B. M: MUC-5 evaluation metrics, in: Proceedings of the Fifth Message Understand-
 685 ing Conference (MUC-5), August 25-27, 1993, <https://doi.org/10.3115/1072017.1072026>, 1993.

686 Coelho, J., Valente, M. T., Milen, L., and Silva, L. L.: Is this GitHub project maintained? Measuring the level of
 687 maintenance activity of open-source projects, *Inf. Software Technol.*, 122, 106274,
 688 <https://doi.org/10.1016/j.infsof.2020.106274>, 2020.

689 Comas, X., Wright, W., Hynek, S. A., Fletcher, R. C., and Brantley, S. L.: Understanding fracture distribution and
 690 its relation to knickpoint evolution in the Rio Icacos watershed (Luquillo Critical Zone Observatory, Puerto Rico)
 691 using landscape-scale hydrogeophysics, *Earth Surf. Processes Landforms*, 44(4), 877-885,
 692 <https://doi.org/10.1002/esp.4540>, 2019.

693 Conrad, O., Bechtel, B., Bock, M., Dietrich, H., Fischer, E., Gerlitz, L., ... and Böhner, J.: System for automated
 694 geoscientific analyses (SAGA) v. 2.1. 4, *Geosci. Model Dev.*, 8(7), 1991-2007, <https://doi.org/10.5194/gmd-8-1991-2015>, 2015.

696 Cresson, R.: A framework for remote sensing images processing using deep learning techniques, *IEEE Geosci.*
 697 *Remote Sens. Lett.*, 16(1), 25-29, <https://doi.org/10.1109/lgrs.2018.2867949>, 2018.

698 Cresson, R. (2022). SR4RS: A tool for super resolution of remote sensing images, *J. Open Res. Software*, 10(1),
 699 <https://doi.org/10.5334/jors.369>, 2022.

700 Cutler, A., Cutler, D. R., and Stevens, J. R.: Random forests, in: Ensemble machine learning: Methods and appli-
 701 cations, edited by: Zhang, C., and Ma, Y., Springer, 157-175, https://doi.org/10.1007/978-1-4419-9326-7_5, 2012.

702 Dong, H., Peacor, D. R., and Murphy, S. F.: TEM study of progressive alteration of igneous biotite to kaolinite
 703 throughout a weathered soil profile, *Geochim. Cosmochim. Acta*, 62(11), 1881-1887,
 704 [https://doi.org/10.1016/s0016-7037\(98\)00096-9](https://doi.org/10.1016/s0016-7037(98)00096-9), 1998.

705 Elghali, A., Benzaazoua, M., Bouzazhah, H., Bussière, B., and Villarraga-Gómez, H.: Determination of the avail-
 706 able acid-generating potential of waste rock, part I: Mineralogical approach, *Appl. Geochem.*, 99, 31-41,
 707 <https://doi.org/10.1016/j.apgeochem.2018.12.010>, 2018

708 Fandrich, R., Gu, Y., Burrows, D., and Moeller, K.: Modern SEM-based mineral liberation analysis, *Int. J. Miner.*
709 *Process.*, 84(1-4), 310-320, <https://doi.org/10.1016/j.minpro.2006.07.018>, 2007.

710 Ferrier, K. L., Kirchner, J. W., Riebe, C. S., and Finkel, R. C.: Mineral-specific chemical weathering rates over
711 millennial timescales: Measurements at Rio Icacos, Puerto Rico, *Chem. Geol.*, 277(1-2), 101-114,
712 <https://doi.org/10.1016/j.chemgeo.2010.07.013>, 2010.

713 Fletcher, R. C., Buss, H. L., and Brantley, S. L.: A spheroidal weathering model coupling porewater chemistry to
714 soil thicknesses during steady-state denudation, *Earth Planet. Sci. Lett.*, 244(1-2), 444-457,
715 <https://doi.org/10.1016/j.epsl.2006.01.055>, 2006.

716 GDAL/OGR contributors: GDAL/OGR Geospatial Data Abstraction Software Library. Zenodo [code],
717 <https://doi.org/10.5281/zenodo.5884351>, 2023.

718 Gillies, S., and others: Rasterio: geospatial raster I/O for Python programmers, GitHub [code],
719 <https://github.com/rasterio/rasterio>, 2019.

720 Gillies, S., van der Wel, C., van den Bossche, J., Taves, M., Arnott, J., and Ward, B. C.: Shapely: Manipulation
721 and analysis of geometric objects in the Cartesian plane. Zenodo [code], <https://doi.org/10.5281/zenodo.5597138>,
722 2023.

723 Goldstein, J. I., Newbury, D. E., Michael, J. R., Ritchie, N. W., Scott, J. H. J., and Joy, D. C.: *Scanning Electron*
724 *Microscopy and X-ray Microanalysis*, 4th Edition, Springer, <https://doi.org/10.1007/978-1-4939-6676-9>, 2018.

725 Gonzalez, C. G., and Woods, R. E.: *Digital Image Processing*, 4th Edition, Pearson, 2018.

726 Goodfellow, B. W., and Hilley, G. E.: Climatic and lithological controls on the structure and thickness of granitic
727 weathering zones, *Earth Planet. Sci. Lett.*, 600, 117890, <https://doi.org/10.1016/j.epsl.2022.117890>, 2022.

728 Goodfellow, B. W., Hilley, G. E., Webb, S. M., Sklar, L. S., Moon, S., and Olson, C. A.: The chemical, mechani-
729 cal, and hydrological evolution of weathering granitoid, *J. Geophys. Res.: Earth Surf.*, 121(8), 1410-1435,
730 <https://doi.org/10.1002/2016jf003822>, 2016.

731 Gottlieb, P., Wilkie, G., Sutherland, D., Ho-Tun, E., Suthers, S., Perera, K., Jenkins, B., Spencer, S., Butcher, A.,
732 and Rayner, J.: Using quantitative electron microscopy for process mineralogy applications, *JOM*, 52, 24-25,
733 <https://doi.org/10.1007/s11837-000-0126-9>, 2000.

734 Grizonnet, M., Michel, J., Poughon, V., Inglada, J., Savinaud, M., and Cresson, R. (2017). Orfeo ToolBox: Open
735 source processing of remote sensing images, *Open Geospatial Data, Software and Stand.*, 2(1), 1-8,
736 <https://doi.org/10.1186/s40965-017-0031-6>, 2017.

737 Gu, Y. Automated scanning electron microscope based mineral liberation analysis. *Journal of Minerals and Mate-*
738 *rials Characterization and Engineering*, 2(1), <https://doi.org/10.4236/jmmce.2003.2100333-41>. 2003.

739 Guo, L., Chehata, N., Mallet, C., and Boukir, S.: Relevance of airborne lidar and multispectral image data for ur-
740 ban scene classification using Random Forests, *ISPRS J. Photogramm. Remote Sens.*, 66(1), 56-66,
741 <https://doi.org/10.1016/j.isprsjprs.2010.08.007>, 2011.

742 Han, S., Löhr, S. C., Abbott, A. N., Baldermann, A., Farkaš, J., McMahon, W., Miliken, K., Rafiei, M., Wheeler,
 743 C., and Owen, M.: Earth system science applications of next-generation SEM-EDS automated mineral mapping,
 744 *Front. Earth Sci.*, 10, 956912, <https://doi.org/10.3389/feart.2022.956912>, 2022.

745 Harlov, D. E., Hansen, E. C., and Bigler, C.: Petrologic evidence for K-feldspar metasomatism in granulite facies
 746 rocks, *Chem. Geol.*, 151(1-4), 373-386, [https://doi.org/10.1016/s0009-2541\(98\)00090-4](https://doi.org/10.1016/s0009-2541(98)00090-4), 1998.

747 Harris, C.R., Millman, K.J., van der Walt, S.J., Gommers, R., Virtanen, P., and Cournapeau, D.: Array program-
 748 ming with NumPy, *Nature*, 585, 357–362. <https://doi.org/10.1038/s41586-020-2649-2>, 2020.

749 Hazen, R. M., Papineau, D., Bleeker, W., Downs, R. T., Ferry, J. M., McCoy, T. J., and Yang, H.: Mineral evolu-
 750 tion, *Am. Mineral.*, 93(11-12), 1693-1720, <https://doi.org/10.2138/am.2008.2955>, 2008.

751 He, H., & Garcia, E. A. Learning from imbalanced data. *IEEE Transactions on knowledge and data engineering*,
 752 21(9), 1263-1284, <https://doi.org/10.1109/TKDE.2008.239>, 2009.

753 Hilton, R. G., and West, A. J.: Mountains, erosion and the carbon cycle, *Nat. Rev. Earth Environ.*, 1(6), 284-299,
 754 <https://doi.org/10.1038/s43017-020-0058-6>, 2020.

755 Hrstka, T., Gottlieb, P., Skala, R., Breiter, K., and Motl, D.: Automated mineralogy and petrology-applications of
 756 Tescan Integrated Mineral Analyzer (TIMA), *J. Geosci.*, 63(1), 47-63, <https://doi.org/10.3190/jgeosci.250>,
 757 2018.

758 Hupp, B. N., and Donovan, J. J.: Quantitative mineralogy for facies definition in the Marcellus Shale (Appala-
 759 chian Basin, USA) using XRD-XRF integration, *Sediment. Geol.*, 371, 16-31,
 760 <https://doi.org/10.1016/j.sedgeo.2018.04.007>

761 Jordahl, K., Van den Bossche, J., Wasserman, J., McBride, J., Gerard, J., Fleischmann, M., ... and Greenhall, A.:
 762 *geopandas/geopandas: v0.12.1*, Zenodo [code], <https://doi.org/10.5281/zenodo.7262879>, 2022.

763 Keulen, N., Malkki, S. N., and Graham, S.: Automated quantitative mineralogy applied to metamorphic rocks,
 764 *Minerals*, 10(1), 47, <https://doi.org/10.3390/min10010047>, 2020.

765 Lanari, P., Vidal, O., De Andrade, V., Dubacq, B., Lewin, E., Grosch, E. G., and Schwartz, S.: XMapTools: A
 766 MATLAB©-based program for electron microprobe X-ray image processing and geothermobarometry, *Comput.*
 767 *Geosci.*, 62, 227-240, <https://doi.org/10.1016/j.cageo.2013.08.010>, 2014.

768 Le Maitre, R. W.: Classification and nomenclature, in: *Igneous rocks: a classification and glossary of terms: rec-*
 769 *ommendations of the International Union of Geological Sciences Subcommission on the Systematics of Igneous*
 770 *Rocks*, edited by: Le Maitre, R. W., Streckeisen, A., Zanettin, B., Le Bas, M. J., Bonin, B., and Bateman, P.,
 771 Cambridge University Press, <https://doi.org/10.1017/CBO9780511535581>, 2002.

772 Li, C., Wang, D., and Kong, L.: Application of machine learning techniques in mineral classification for scanning
 773 electron microscopy-energy dispersive X-ray spectroscopy (SEM-EDS) images, *J. Pet. Sci. Eng.*, 200, 108178,
 774 <https://doi.org/10.1016/j.petrol.2020.108178>, 2021.

775 Li, L., Lee, P. K. K., Tsui, Y., Tham, L. G., and Tang, C. A.: Failure process of granite, *Int. J. Geomech.*, 3(1), 84-
 776 98, [https://doi.org/10.1061/\(ASCE\)1532-3641\(2003\)3:1\(84\)](https://doi.org/10.1061/(ASCE)1532-3641(2003)3:1(84)), 2003.

777 Mahabadi, O. K., Randall, N. X., Zong, Z., and Grasselli, G.: A novel approach for micro-scale characterization
 778 and modeling of geomaterials incorporating actual material heterogeneity, *Geophys. Res. Lett.*, 39(1),
 779 <https://doi.org/10.1029/2011gl050411>, 2012.

780 Malac, M., Calzada, J. A. M., Salomons, M., Homeniuk, D., Price, P., Cloutier, M., ... and Egerton, R.: NanoMi:
 781 An open source electron microscope hardware and software platform, *Micron*, 163, 103362,
 782 <https://doi.org/10.1016/j.micron.2022.103362>, 2022.

783 Marra, W. A., van de Grint, L., Alberti, K., and Karssenberg, D. : Using GIS in an Earth Sciences field course for
 784 quantitative exploration, data management and digital mapping, *J. Geogr. Higher Educ.*, 41(2), 213-229,
 785 <https://doi.org/10.1080/03098265.2017.1291587>, 2017.

786 Maxwell, A. E., Warner, T. A., and Fang, F.: Implementation of machine-learning classification in remote sensing:
 787 An applied review, *Int. J. Remote Sens.*, 39(9), 2784-2817, <https://doi.org/10.1080/01431161.2018.1433343>,
 788 2018.

789 McInerney, D., and Kempeneers, P.: Virtual Rasters and Raster Calculations. in: *Open Source Geospatial Tools:*
 790 *Applications in Earth Observation, Earth Systems Data and Models.* Springer, [https://doi.org/10.1007/978-3-319-](https://doi.org/10.1007/978-3-319-01824-9_11)
 791 [01824-9_11](https://doi.org/10.1007/978-3-319-01824-9_11), 2015.

792 Murphy, S. F., Brantley, S. L., Blum, A. E., White, A. F., and Dong, H.: Chemical weathering in a tropical water-
 793 shed, Luquillo Mountains, Puerto Rico: II. Rate and mechanism of biotite weathering, *Geochim. Cosmochim.*
 794 *Acta*, 62(2), 227-243, [https://doi.org/10.1016/s0016-7037\(97\)00336-0](https://doi.org/10.1016/s0016-7037(97)00336-0), 1998.

795 Newbury, D. E., and Ritchie, N. W.: Elemental mapping of microstructures by scanning electron microscopy-en-
 796 ergy dispersive X-ray spectrometry (SEM-EDS): extraordinary advances with the silicon drift detector (SDD), *J.*
 797 *Anal. At. Spectrom.*, 28(7), 973-988, <https://doi.org/10.1039/c3ja50026h>, 2013.

798 Nikonow, W., and Rammlmair, D.: Automated mineralogy based on micro-energy-dispersive X-ray fluorescence
 799 microscopy (μ -EDXRF) applied to plutonic rock thin sections in comparison to a mineral liberation analyzer, *Ge-*
 800 *osci. Instrum. Methods Data Syst.*, 6(2), 429-437, <https://doi.org/10.5194/gi-6-429-2017>, 2017.

801 Nikonow, W., Rammlmair, D., Meima, J. A., and Schodlok, M. C.: Advanced mineral characterization and petro-
 802 graphic analysis by μ -EDXRF, LIBS, HSI and hyperspectral data merging, *Mineral. Petrol.*, 113, 417-431,
 803 <https://doi.org/10.1007/s00710-019-00657-z>, 2019.

804 Orlando, J., Comas, X., Hynek, S. A., Buss, H. L., and Brantley, S. L.: Architecture of the deep critical zone in
 805 the Río Icacos watershed (Luquillo Critical Zone Observatory, Puerto Rico) inferred from drilling and ground
 806 penetrating radar (GPR), *Earth Surf. Processes Landforms*, 41(13), 1826-1840, <https://doi.org/10.1002/esp.3948>,
 807 2016.

808 Ortolano, G., Visalli, R., Godard, G., and Cirrincione, R.: Quantitative X-ray Map Analyser (Q-XRMA): A new
 809 GIS-based statistical approach to Mineral Image Analysis, *Comput. Geosci.*, 115, 56-65,
 810 <https://doi.org/10.1016/j.cageo.2018.03.001>, 2018.

811 Ortolano, G., Zappalà, L., and Mazzoleni, P.: X-Ray Map Analyser: A new ArcGIS® based tool for the quantita-
812 tive statistical data handling of X-ray maps (Geo-and material-science applications), *Comput. Geosci.*, 72, 49-64,
813 <https://doi.org/10.1016/j.cageo.2014.07.006>, 2014.

814 Pedregosa, F., Varoquaux, G., Gramfort, A., Michel, V., Thirion, B., Grisel, O., ... and Duchesnay, É.: Scikit-
815 learn: Machine learning in Python, *J. Mach. Learn. Res.*, 12, 2825-2830,
816 <https://doi.org/10.48550/arxiv.1201.0490>, 2011.

817 Perkins, D.: Mineralogy, Open Educational Resources, University of North Dakota,
818 <https://doi.org/10.31356/oers025>, 2020.

819 Pirrie, D., and Rollinson, G. K.: Unlocking the applications of automated mineral analysis, *Geol. Today*, 27(6),
820 226-235, <https://doi.org/10.1111/j.1365-2451.2011.00818.x>, 2011.

821 Přikryl, R.: Assessment of rock geomechanical quality by quantitative rock fabric coefficients: limitations and
822 possible source of misinterpretations, *Eng. Geol.*, 87(3-4), 149-162,
823 <https://doi.org/10.1016/j.enggeo.2006.05.011>, 2006.

824 Probst, P., Wright, M. N., and Boulesteix, A. L.: Hyperparameters and tuning strategies for random forest, *Wiley*
825 *Interdiscip. Rev.: Data Min. Knowl. Discovery*, 9(3), e1301, <https://doi.org/10.1002/widm.1301>, 2019.

826 Rafiei, M., Löhr, S., Baldermann, A., Webster, R., and Kong, C.: Quantitative petrographic differentiation of de-
827 trital vs diagenetic clay minerals in marine sedimentary sequences: Implications for the rise of biotic soils, *Pre-*
828 *cambrian Research*, 350, 105948, <https://doi.org/10.1016/j.precamres.2020.105948>, 2020.

829 Ramachandran, R., Bugbee, K., and Murphy, K.: From open data to open science, *Earth Space Sci.*, 8(5),
830 e2020EA001562, <https://doi.org/10.1029/2020EA001562>, 2021.

831 Raza, A., and Capretz, L. F.: Contributors preference in open source software usability: An empirical study, *arXiv*
832 [preprint], <https://doi.org/10.48550/arXiv.1507.06882>, 24 July 2015.

833 Riebe, C. S., Kirchner, J. W., and Finkel, R. C.: Long-term rates of chemical weathering and physical erosion
834 from cosmogenic nuclides and geochemical mass balance, *Geochim. Cosmochim. Acta*, 67(22), 4411-4427,
835 [https://doi.org/10.1016/s0016-7037\(03\)00382-x](https://doi.org/10.1016/s0016-7037(03)00382-x), 2003.

836 Reed, M. M., Ferrier, K. L., Nachlas, W. O., Schneider, B., Arson, C., Xu, T., Shen, X., West, N.: Supplement to
837 “A free, open-source method for automated mapping of quantitative mineralogy from energy-dispersive X-ray
838 spectroscopy scans of rock thin sections”, *Zenodo* [code and datasets], <https://doi.org/10.5281/zenodo.10912628>,
839 2024.

840 Schulz, B., Sandmann, D., and Gilbricht, S.: SEM-based automated mineralogy and its application in geo-and
841 material sciences, *Minerals*, 10(11), 1004, <https://doi.org/10.3390/min10111004>, 2020.

842 Shen, X., Arson, C., Ferrier, K. L., West, N., and Dai, S.: Mineral weathering and bedrock weakening: Modeling
843 microscale bedrock damage under biotite weathering, *J. Geophys. Res.: Earth Surf.*, 124(11), 2623-2646,
844 <https://doi.org/10.1029/2019jf005068>, 2019.

845 Speer, J. A. (1984). Micas in igneous rocks, *Rev. Mineral. Geochem.*, 13(1), 299-356.

846 Stallard, R. F., and Murphy, S. F.: Water quality and mass transport in four watersheds in eastern Puerto Rico.
 847 Water quality and landscape processes of four watersheds in eastern Puerto Rico. US Geol. Surv. Prof. Pap.,
 848 1789, 113-152. <https://doi.org/10.3133/pp1789E>, 2012.

849 Sutherland, D., Gottlieb, P., Jackson, R., Wilkie, G., & Stewart, P. Measurement in section of particles of known
 850 composition. Minerals Engineering, 1(4), 317-326, [https://doi.org/10.1016/0892-6875\(88\)90021-0](https://doi.org/10.1016/0892-6875(88)90021-0), 1988.

851 Sutherland, D. N., and Gottlieb, P. Application of automated quantitative mineralogy in mineral processing. Min-
 852 erals Engineering, 4(7-11), 753-762, [https://doi.org/10.1016/0892-6875\(91\)90063-2](https://doi.org/10.1016/0892-6875(91)90063-2), 1991.

853 Tapponnier, P., and Brace, W. F.: Development of stress-induced microcracks in Westerly granite. In: Interna-
 854 tional Journal of Rock Mechanics and Mining Sciences & Geomechanics Abstracts, [https://doi.org/10.1016/0148-](https://doi.org/10.1016/0148-9062(76)91937-9)
 855 [9062\(76\)91937-9](https://doi.org/10.1016/0148-9062(76)91937-9), 1976.

856 Tarquini, S., and Favalli, M.: A microscopic information system (MIS) for petrographic analysis, Comput. Ge-
 857 osci., 36(5), 665-674, <https://doi.org/10.1016/j.cageo.2009.09.017>, 2010.

858 Ündül, Ö.: Assessment of mineralogical and petrographic factors affecting petro-physical properties, strength and
 859 cracking processes of volcanic rocks, Eng. Geol., 210, 10-22, <https://doi.org/10.1016/j.enggeo.2016.06.001>,
 860 2016.

861 Wahrhaftig, C.: Stepped topography of the southern Sierra Nevada, California, Geol. Soc. Am. Bull., 76(10),
 862 1165-1190, [https://doi.org/10.1130/0016-7606\(1965\)76\[1165:stotss\]2.0.co;2](https://doi.org/10.1130/0016-7606(1965)76[1165:stotss]2.0.co;2), 1965.

863 White, A. F., Blum, A. E., Schulz, M. S., Vivit, D. V., Stonestrom, D. A., Larsen, M., Murphy, S., and Eberl, D.:
 864 Chemical weathering in a tropical watershed, Luquillo Mountains, Puerto Rico: I. Long-term versus short-term
 865 weathering fluxes, Geochim. Cosmochim. Acta, 62(2), 209-226, [https://doi.org/10.1016/s0016-7037\(97\)00335-9](https://doi.org/10.1016/s0016-7037(97)00335-9),
 866 1998.

867 Xu, T., Shen, X., Reed, M., West, N., Ferrier, K. L., and Arson, C.: Anisotropy and microcrack propagation in-
 868 duced by weathering, regional stresses and topographic stresses, J. Geophys. Res.: Solid Earth, 127(7),
 869 e2022JB024518, <https://doi.org/10.1029/2022JB024518>, 2022.

870